FUEL PIN
PRELIMINARY DESIGN
Nuclear Engineering – Politecnico di Milano

Simone Pagliuca, Tommaso Pirola, Lisa Raffuzzi, Riccardo Ronchi, Darien Shabi

simone1.pagliuca@mail.polimi.it,
tommaso1.pirola@mail.polimi.it,
lisa.raffuzzi@mail.polimi.it,
riccardo3.ronchi@mail.polimi.it,
darien.shabi@mail.polimi.it

Course: Nuclear Design and Technologies
Academic year: 2024/2025

ABSTRACT: This report presents the preliminary design and verification of a fuel pin for a sodium-cooled fast reactor. The analysis focuses on determining cladding thickness, the size of the fuel-cladding gap, and the plenum height while ensuring compliance with design limits and safety margins. The main assumptions, approximations, and conclusions are discussed.

Key-words: Fuel Pin, Lead Cooled, Plenum, Cladding Thickness

CONTENTS

1 INTRODUCTION

This report presents the preliminary design and verification of a fuel pin for a sodium-cooled fast reactor, as specified in the assignment. The analysis encompasses calculations for material properties, thermal-hydraulic conditions, and mechanical stress limits.

The robustness of the developed models is verified, and the assumptions made throughout the process are clearly justified.

1.1 Problem Description

The fuel pin design problem involves the following tasks:

- ↪ Determining the cladding thickness, the fuel-cladding gap size, and the plenum height.

- ↪ Verifying the design against specified limits, including fuel melting, cladding temperature, yielding, and rupture time due to thermal creep.

- ↪ Identifying critical design aspects if the irradiation time is doubled.

Most of the project specifications and material properties were provided. For missing information, data were sourced either from previous handouts related to a similar reactor or from relevant literature.

1.2 Assumptions

The following assumptions were adopted to address the given problem:

Steady-State Solution for Gas in Grains

- ↪ The rate equation for the gas within the grains (PDE) was analyzed under steady-state conditions. This approach was chosen because the objective is to size the plenum for a 1-year operation without focusing on the temporal evolution of the function.

Fission Rate Calculation

- ↪ The fission rate was determined using the formula:

$$\text{Fission Rate} = \Sigma_f \Phi_{\text{avg}}$$

- ↪ The macroscopic fission cross section was derived using data from the JANIS database.

- ↪ The average flux was calculated by assuming a uniform power and flux profile.

Material Properties and Geometry

↪ Material properties were treated as temperature-dependent and modeled using the provided empirical correlations.

↪ Axial power and neutron flux profiles were assumed to remain constant over time.

↪ Initial helium pressure and temperature in the fuel-cladding gap were considered as specified.

↪ Simplifications in geometry were introduced, such as neglecting axial deformation, to facilitate computation.

2 VERIFICATION OF MODELS

Each component of the analysis code was validated to confirm it behaves as expected under the defined conditions. The verification process is detailed in the following sections.

3 THERMAL–HYDRAULICS ANALYSIS

Preliminary checks were performed to validate the coolant properties, including density, viscosity, and thermal conductivity, at the coolant inlet temperature.

The heat transfer coefficient between the coolant and cladding was calculated using Nusselt number correlations, ensuring accurate representation of the thermal exchange process.

Figure 1 presents the axial power profile. The computed heat transfer coefficient in the cold geometry was determined to be:

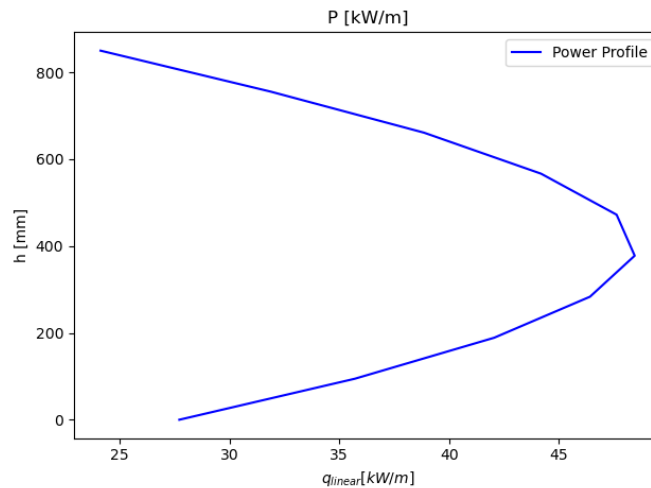$$\alpha_{\text{coolant}} = 139.98 \, \frac{\text{kW}}{\text{m}^2 \cdot \text{K}}$$

Figure 1: Axial power profile used in the thermal-hydraulics analysis.

4 TEMPERATURE PROFILES

Radial and axial temperature profiles were computed for the cold geometry to verify the profile's shape and to ensure that the calculated values were reasonable.

A temperature map of the fuel rod was created. For each node along the axial direction, the temperature increase in the coolant was first computed based on the heat generated in the fuel. Using this, the temperature at the coolant-cladding interface was determined by applying the heat transfer coefficient, calculated from provided correlations.

For the cladding, a linear temperature profile was assumed to estimate the temperature at the cladding-gas interface. For the gap and the fuel, multiple temperature points were calculated along the radial direction. At each step, the material properties were updated to reflect the temperature of the previous step. The inner void was assumed to be at the same temperature as the inner surface of the fuel.

The results provided an initial validation of the temperature distribution behavior, confirming that the trends were consistent and the values were within expected ranges before proceeding with further analysis.

Figure 2 illustrates the axial temperature profile at the interfaces, while Figure 3 shows the radial temperature profiles at the bottom, middle, and top of the fuel rod.
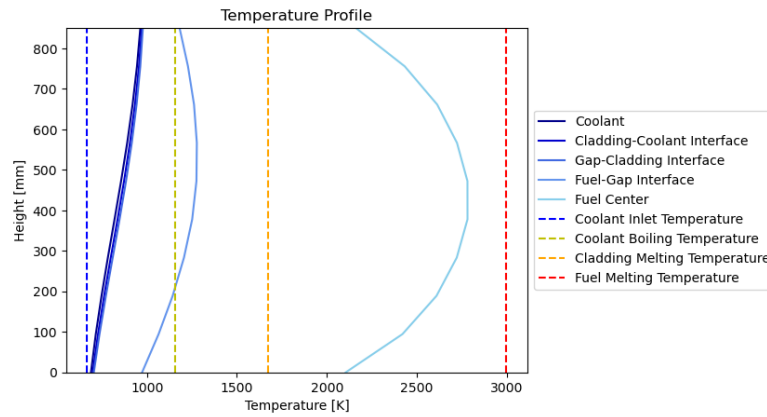

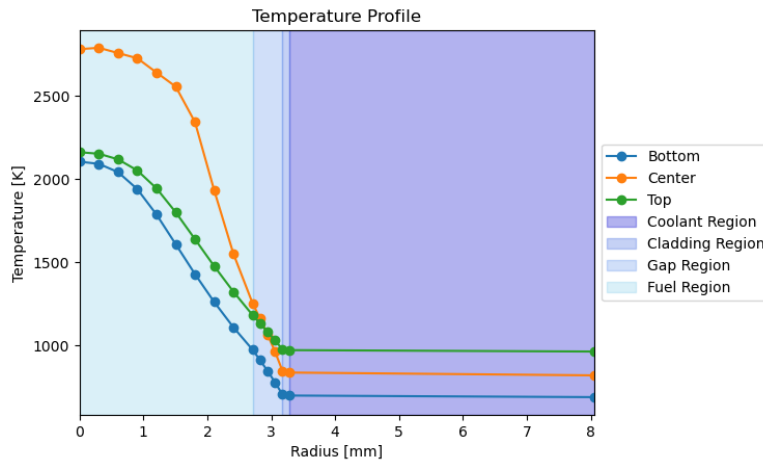Figure 2: Axial temperature profile for cold geometry.

Figure 3: Radial temperature profiles for cold geometry at the bottom, middle, and top of the fuel rod.

5 THERMAL EXPANSION ANALYSIS

The fuel and cladding form a coupled system, with the gap between them playing a critical role in heat transfer, mechanical interactions, and overall reactor safety. Accurate evaluation of thermal expansion is essential to ensure efficient operation and structural integrity of the reactor core. These calculations account for material-specific thermal expansion coefficients and the temperature distributions derived from operational data.

5.1 Axial Temperature Profile of the Fuel and Axial Profile of Fuel Radius (Cold vs. Hot Geometry)

The axial temperature profile of the fuel under hot operational conditions is shown in Figure 4. This profile provides insight into the temperature distribution along the fuel height, which is essential for evaluating thermal stresses and expansion. The corresponding axial profile of the fuel radius, depicted in Figure 5, demonstrates that the material's expansion aligns closely with the temperature distribution.
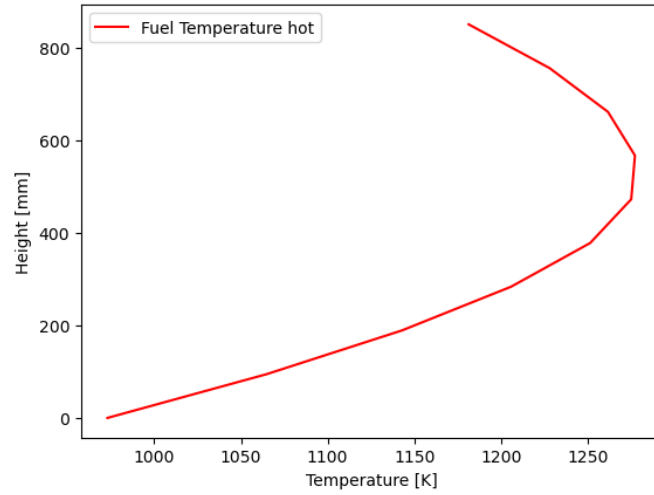
Figure 4: Axial temperature profile of the fuel under hot operational conditions.
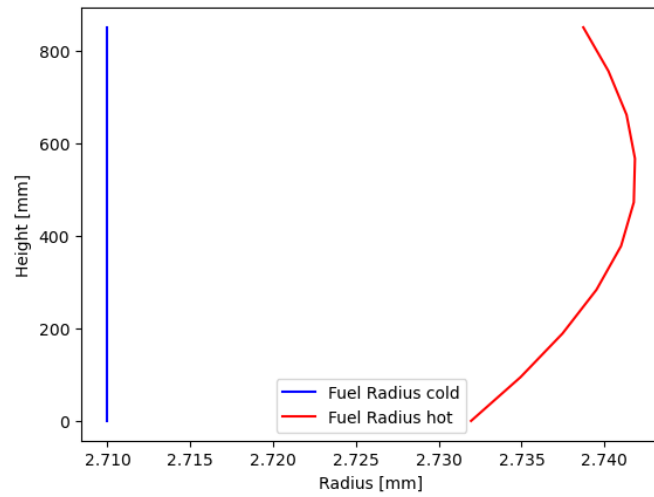
Figure 5: Axial profile of the fuel radius (cold vs. hot geometry).

5.2 Axial Temperature Profile of the Inner and Outer Cladding (Cold vs. Hot Geometry)

The axial temperature profiles of the cladding's inner and outer surfaces illustrate the thermal distribution along its height. Figure 6 highlights the uniform expansion of the cladding along its axial height. The temperature difference between the inner and outer surfaces remains consistent, as shown in Figure 7.
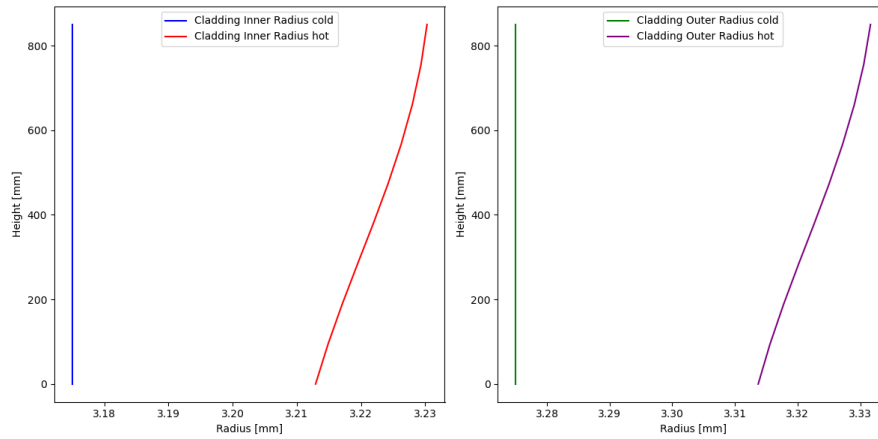
Figure 6: Axial temperature profile of the cladding (cold vs. hot geometry).
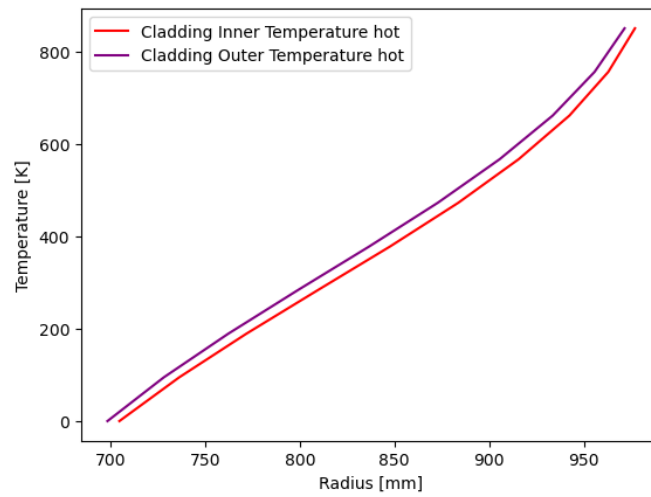
Figure 7: Axial profile of the cladding radius (cold vs. hot geometry).

5.3 Gap and Cladding Thickness Along Axial Height

The evolution of the fuel-cladding gap due to differential expansion is presented in Figure 8. This parameter significantly influences heat transfer efficiency and mechanical interactions in the reactor core. While the change in cladding thickness with temperature is relatively minor compared to the change in radius, it remains a critical factor for evaluating structural integrity.
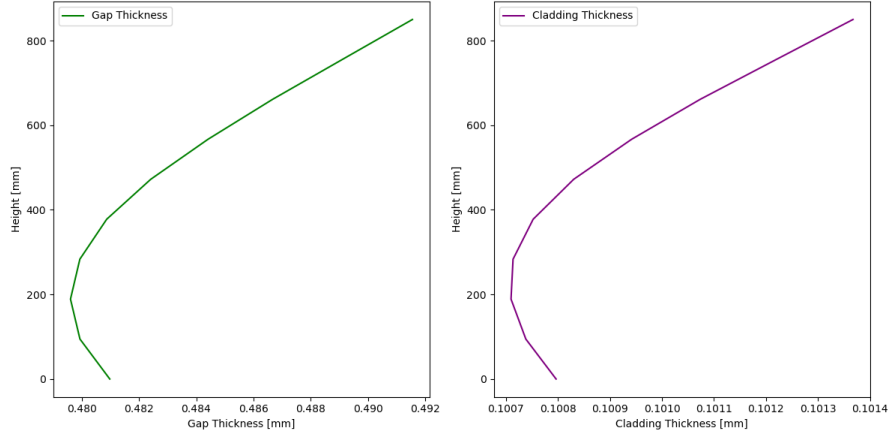
Figure 8: Gap and cladding thickness along the axial height.

5.4 Discussion

As anticipated, the fuel exhibits more pronounced thermal expansion due to its higher temperature gradient compared to the cladding. This results in a reduction of the gap between the fuel and cladding, enhancing thermal coupling. However, careful management of this reduced gap is necessary to prevent mechanical interactions that could compromise the system's structural integrity.

6 VOID SWELLING

The volumetric void swelling of the cladding was evaluated using a provided correlation. Assuming isotropic swelling, the radial expansion was estimated as one-third of the volumetric expansion:

$$\Delta R_{\text{radial}} = \frac{1}{3} \Delta V_{\text{volumetric}}$$

Figure 9 illustrates the swelling of the cladding along the axial direction. As expected, swelling occurs only within a specific temperature range. At lower temperatures, swelling is negligible, while at higher temperatures, increased atomic mobility leads to recombination, which limits the extent of swelling.
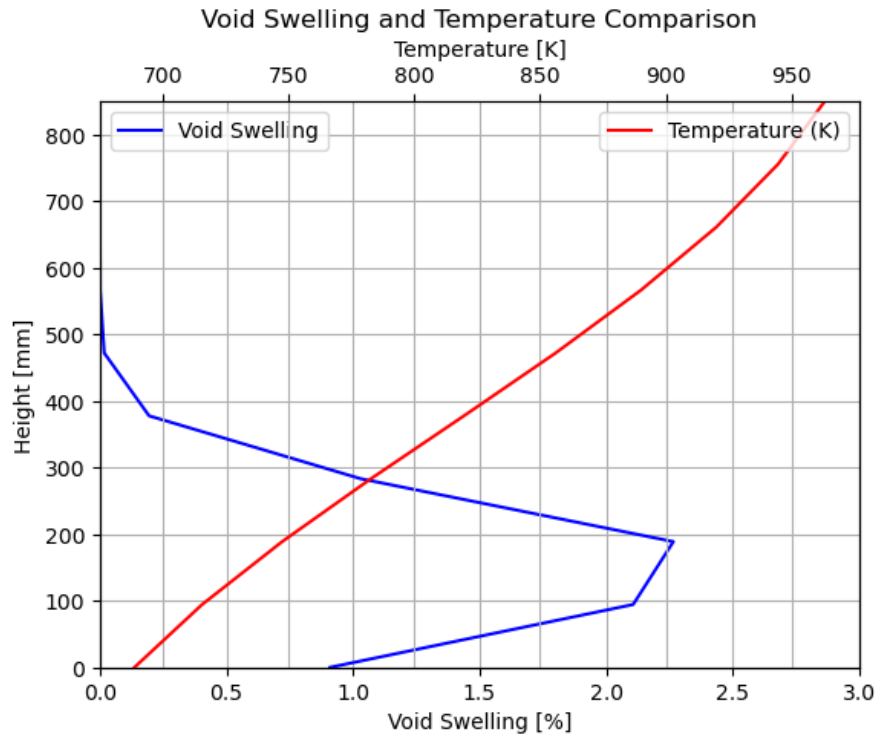
Figure 9: Cladding swelling due to void formation along the axial direction.

7 FISSION GAS BEHAVIOUR

This section examines the behaviour of the two primary gases produced by fission events, Xenon (Xe) and Krypton (Kr), focusing on their impact on design parameters such as the plenum height.

Both Xe and Kr are chemically inert gases with a combined fission yield of approximately 30% (including contributions from other fast-decay fission products that convert into Xe and Kr within minutes).

Fission events lead to a constant production of fission gas atoms distributed throughout the fuel, resulting in two key phenomena: Fuel Gaseous Swelling and Fission Gas Release (FGR).

7.1 Fission Gas Release

Through diffusion, a portion of the fission gas produced in the fuel is released into the plenum. This release "pollutes" the helium initially present in the plenum, reducing its thermal conductivity and increasing the internal pressure of the pin as additional gas moles accumulate within a fixed volume.

These phenomena occur continuously under irradiation and influence the thermo-mechanical behaviour of the fuel pin in a highly non-linear manner. Accurate prediction and control are essential for safe operation.

The problem is addressed using Rate Theory Equations coupled with Cluster Dynamics considerations. The phenomenon is modeled at the grain scale, which serves as the domain for the analysis. The following equations are solved:

Total Gas Production   The total amount of gas produced is governed by a simple ordinary differential equation:

$$\frac{dP}{dt} = y \cdot \dot{F} \tag{1}$$

where:

- $P \left(\frac{\text{at}}{\text{m}^3} \right)$: Gas produced.

- y: Fission yield (combined for Xe and Kr).

- $\dot{F}$: Fission rate.

Intra-granular Gas Behaviour   The intra-granular behaviour of fission gases is described by:

$$\frac{dG_M}{dt} = D_{\text{eff}} \cdot \nabla^2 G_M + y \cdot \dot{F} \tag{2}$$

where:

- $G_M \left(\frac{\text{at}}{\text{m}^3} \right)$: Gas retained by the grain.

- D_{eff}: Effective diffusivity, encompassing all relevant phenomena.

7.2 Main Assumptions, Data, and Hypotheses

- **Domain size**: Grain size $d_g = 10 \, \mu$m.

- **Diffusivity model**: Matzke (1980):

$$D_{\text{eff}} \, [\text{m}^2/\text{s}] = D_0 \cdot \exp\left(-\frac{Q}{T}\right) \tag{3}$$

  where $D_0 = 5 \cdot 10^{-8} \, \text{m}^2/\text{s}$, $Q = 40262$, and T is the temperature in Kelvin.

- **Reference temperature**: Average of the three main axial temperatures (first slice, midplane, last slice).

- **Fission yield**: Combined yield for Xe and Kr, $y = 30$%.

- **Fission rate**: $\dot{F} = \Sigma_f \cdot \phi_{\text{avg}}$, where Σ_f is the macroscopic fission cross section and ϕ_{avg} is the average neutron flux.

- **Initial conditions**: $P(0) = 0$, $G_M(0) = 0$.

- **Boundary conditions** (Booth, 1957):

    - Surface: Perfect sink, $G_M(a) = 0$.

- Center: Symmetry, $\frac{dG_M(0)}{dr} = 0$.

  – **Steady-state assumption**: Given the short timescale of the phenomenon, the system is assumed to stabilize quickly. The time derivative is neglected for the steady-state solution.

The solution should look like the following figure:
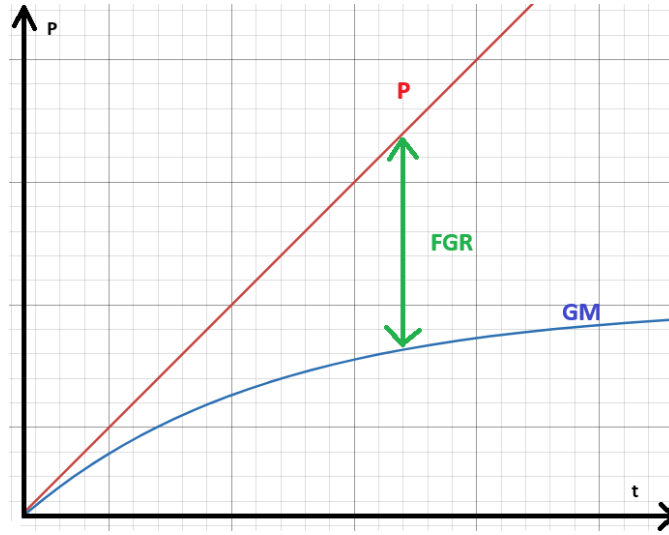
Figure 10: Overall Fission Gas Concentration.

7.3 Results and Comments

7.3.1 Total Gas Produced

The total amount of gas produced is computed by solving the equation:

$$\frac{dP}{dt} = Y_f \cdot \dot{F} \tag{4}$$

At $t = 360$ days, the total gas produced is:

$$P(1y) = 1.23 \cdot 10^{27} \, \text{at/m}^3$$
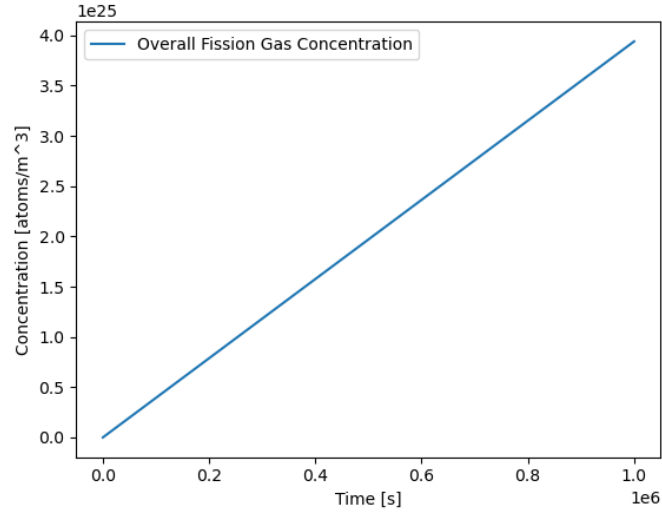
Figure 11: Overall Fission Gas Concentration.

7.3.2 Gas Retained by Grain

The spatial distribution of retained gas, G_M, is shown below:
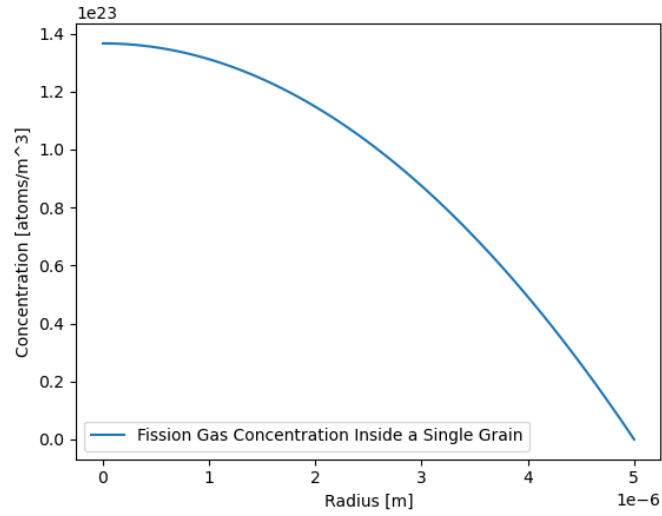
Figure 12: Fission Gas Concentration Inside a Single Grain.

Integrating this curve across the grain domain and multiplying by the number of grains per pellet and pellets per pin provides the total amount of gas retained in the fuel.

The difference between the total gas produced and the gas retained gives the total Fission Gas Release (FGR).

Table 1: Summary of Computed Parameters and Quantities

Parameter	Value
Σ_f	$0.027\ \text{cm}^{-1}$
ϕ_{avg}	$4.87 \cdot 10^{15}\ \text{n/cm}^2 \cdot \text{s}$
$\dot{F}$	$1.31 \cdot 10^{20}\ \text{fissions/m}^3 \cdot \text{s}$
T_{avg}	$2349.25\ \text{K}$
D_{eff}	$1.8 \cdot 10^{-15}\ \text{m}^2/\text{s}$
$P(1y)$	$1.23 \cdot 10^{27}\ \text{at/m}^3$
$G_M(1y)$	$1.10 \cdot 10^{25}\ \text{at/m}^3$
FGR	$1.21 \cdot 10^{27}\ \text{at/m}^3$

7.4   Impact on the Design

The FGR contributes to increased internal pin pressure, which may affect cladding integrity. The maximum allowable internal pressure is set at $5\,\text{MPa}$. Using the ideal gas law:

$$p \cdot V = n \cdot R \cdot T \tag{5}$$

the effect of different plenum heights on internal pressure is evaluated.
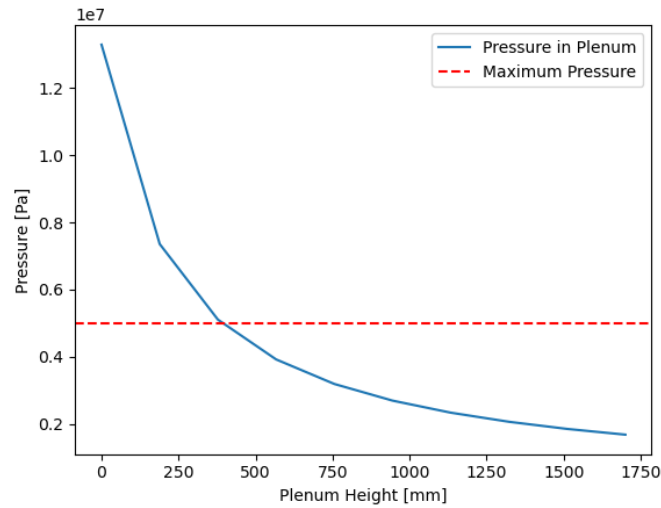
Figure 13: Pressure in Plenum vs. Plenum Height.

Additionally, FGR reduces the thermal conductivity of the gap filling gas, increasing the fuel temperature. This temperature rise enhances FGR, creating a positive feedback loop. Iterative calculations account for this feedback to reach stable temperature and FGR values.

8   RESTRUCTURING

After transitioning from cold geometry to hot geometry and accounting for thermal expansion, the fuel restructuring process must be considered. This involves assumptions about the

radii of columnar and equiaxed regions as well as the corresponding densities in these regions. According to Holander's book, the temperature boundaries are set at 1800ºC for the columnar region and 1600ºC for the equiaxed region. Regarding densities, the as-fabricated region retains its original density, while the equiaxed region is assumed to have 95% of the theoretical density (TD) and the columnar region 98% of TD.

Initially, the columnar and equiaxed radii are evaluated at 1800ºC and 1600ºC, respectively, based on a temperature map. This map provides temperature values at various heights along the fuel pin and utilizes a precise function to determine the temperature at any position within the previously developed 3D model.

Once the columnar and equiaxed radii are determined, the void radius is calculated. The as-fabricated region corresponds to the remaining portion of the fuel outer radius after subtracting the equiaxed region. The following equation is used to estimate the void formation radius:

$$R_{\text{void}} = \sqrt{R_{\text{col}}^2 - R_{\text{eq}}^2 \cdot \left(\frac{\rho_{\text{AS}}}{\rho_{\text{col}}}\right) + \left(R_{\text{eq}}^2 - R_{\text{col}}^2\right) \cdot \left(\frac{\rho_{\text{eq}}}{\rho_{\text{AS}}}\right)} \tag{6}$$

Finally, the relationship between height and radius is plotted to illustrate the restructuring phenomenon and highlight the axial position dependence (z-axis) of the fuel pin. Figure 14 shows the restructuring effect, with a particular focus on cladding swelling due to void formation.
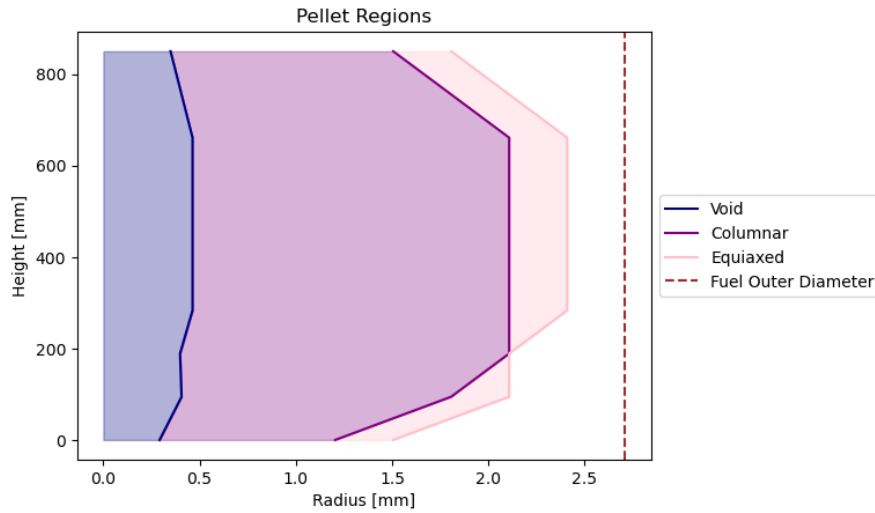
Figure 14: Cladding swelling due to void formation.

9 MECHANICAL ANALYSIS – STRESS ASSESSMENT

9.1 Introduction

This section focuses on the mechanical analysis of the cladding, evaluating stresses to ensure compliance with safety limits during operation. The analysis includes stress computations based on the Mariotte and Lamé criteria, an assessment of plastic strain potential, and an evaluation of rupture time due to thermal creep.

9.2 Methodology

The stress distribution in the cladding was calculated using elasticity equations for cylindrical geometries, under the assumptions of orthocylindricity and axial symmetry.

9.2.1 Mariotte Criterion

↪ Evaluates the hoop stress at the mid-wall of the cladding.

↪ Used to check for yielding. Preliminary calculations indicated that the Mariotte stress is slightly higher than the Lamé stress, although the latter imposes stricter criteria.

9.2.2 Lamé Criterion

↪ Considers radial, hoop, and axial stresses.

↪ The radial stress is computed using the pipe equation with a superposition solution:

$$\frac{d}{dr}\left(r^3 \cdot \frac{d\sigma_r(r)}{dr}\right) + \frac{\alpha E}{1-\nu} \cdot \frac{dT(r)}{dr} = 0 \tag{7}$$

Using equilibrium relations, the hoop stress is determined as:

$$\sigma_\theta = \sigma_r + \frac{d\sigma_r}{dr}$$

↪ The Tresca criterion is applied for verification, ensuring compliance with yield and ultimate strength limits. The Lamé criterion was found to impose limits approximately 33% stricter than the Mariotte criterion.

9.2.3 Plastic Strain Check

↪ Plastic strain is flagged if either criterion predicts stresses exceeding the yield strength.

↪ No significant plastic strain was observed when both criteria were satisfied.

9.2.4 Thermal Creep (Time to Rupture)

↪ The rupture time due to thermal creep was evaluated using the Larson-Miller Parameter (LMP), based on operating stresses and temperatures.

↪ Even under conservative assumptions, the calculated time to rupture showed sufficient margins, indicating minimal risk of creep-related failure.

9.3 Results and Conclusion

9.3.1 Stresses from Mariotte and Lamé

↪ Both criteria confirmed that the stresses remain below critical limits.

↪ While the Mariotte stress tends to be marginally higher, it remains within safe bounds. Lamé's stricter limits provide an additional safety margin.

9.3.2 Plastic Strain

↪ No significant plastic strain was observed, confirming that the cladding operates within the elastic regime under specified conditions.

9.3.3 Time to Rupture

↪ The LMP-based calculation indicated that the cladding's operational life significantly exceeds the irradiation period, even under conservative conditions.

These analyses validate the mechanical reliability of the cladding in the initial design. The results demonstrate that the proposed design is safe and robust, with sufficient margins for long-term operation. Further refinement of the design will allow for additional verification and optimization.

10 OTHER EFFECTS

Additional phenomena, such as Plutonium redistribution and helium embrittlement, are considered to provide a broader understanding of the fuel pin's behavior.

10.1 Plutonium Redistribution

As a consequence of restructuring, it became necessary to investigate the phenomenon of Plutonium redistribution. During restructuring, distinct zones form within the fuel element:

  – **Central void**: Pores migrate, leading to mass displacement outward.

  – **Columnar grains**: Caused by pore migration and density changes.

  – **Equiaxed grains**: Formed by grain growth at high temperatures.

  – **As-fabricated zone**: A region where the temperature is too low to cause significant changes.

These zones exhibit differences in density and porosity, with the fuel reaching up to 98–99% of its theoretical density (TD). This density variation leads to a redistribution of Plutonium concentration across the zones, which initially had a uniform concentration of 29%.

Plutonium becomes enriched in the central (columnar) zone, followed by a decrease (reaching a minimum) in the equiaxed zone. In the as-fabricated zone, the concentration stabilizes back to the initial value. This redistribution is driven by Plutonium's high activation energy, which enables migration within the fuel.

To evaluate how Plutonium redistribution varies due to thermal expansion and restructuring, we employed the following formula (from the provided handouts, Hot Effects Analysis, V):

$$\frac{q'''(r)}{q_0} = \frac{c(r)}{c_0} = 1 + D\left\{\exp\left[-2\alpha\left(\frac{r-r^*}{R_{\mathsf{fo}}}\right)\right] - 2\cdot\exp\left[-\alpha\left(\frac{r-r^*}{R_{\mathsf{fo}}}\right)\right]\right\} \tag{8}$$

where:

- $D = 0.01$: Redistribution factor (from handouts),

- $\alpha = 10$: Exponential parameter (from handouts),

- $r^* = 0.207 \cdot R_{\text{fo}}$: Empirical constant ensuring conservation of Plutonium,

- $c(r)$: Radial Plutonium concentration [g/cm^3],

- c_0: Initial Plutonium concentration.

This equation models the radial variation of Plutonium concentration, accounting for the interplay of thermal and structural effects. Graphically, the results highlight the key phenomena associated with Plutonium redistribution.

Figure 15 illustrates the restructuring of the fuel element and the formation of distinct zones during irradiation. Figure 16 shows the radial Plutonium concentration profile, normalized relative to the initial concentration.
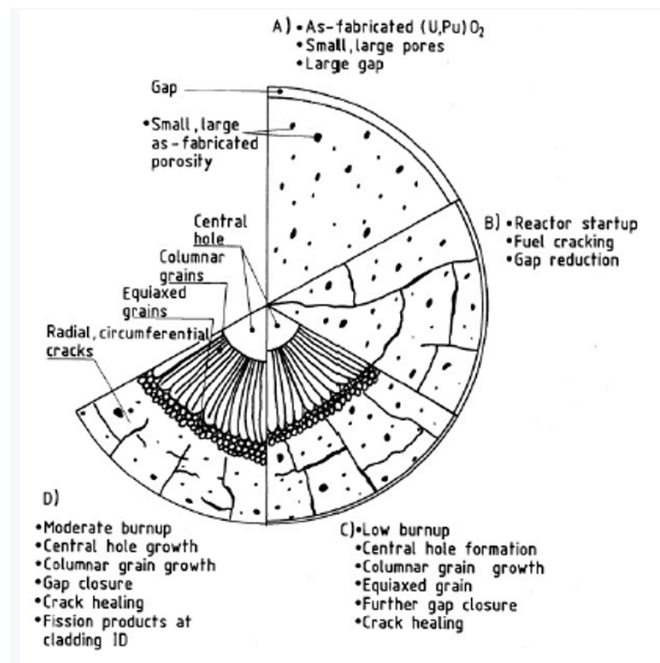

Figure 15: Restructuring of fuel elements and formation of zones during irradiation.
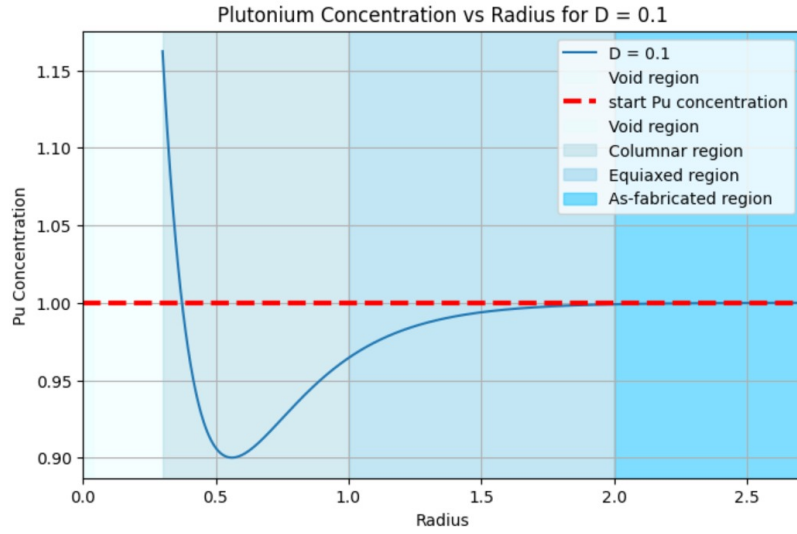
Figure 16: Radial distribution of Plutonium concentration (relative to the starting concentration) within the fuel structure.

10.2 Helium Embrittlement

10.2.1 Helium Production Evaluation

Helium production within the cladding material during reactor operation is primarily driven by neutron interactions with isotopes present in the cladding alloy. The following reactions contribute significantly to helium generation:

- ^{58}Ni(n,α)^{55}Fe (fast neutrons)

- ^{59}Ni(n,γ)^{59}Ni $\rightarrow$^{59}Ni(n,α)^{56}Fe (thermal neutrons)

- ^{10}B(n,α)^{7}Li (thermal and fast neutrons)

- ^{56}Fe(n,α)^{53}Cr (fast neutrons)

- ^{52}Cr(n,α)^{49}Ti (fast neutrons)

The time-dependent helium production rate was calculated using Bateman equations, accounting for both isotopic abundance and neutron flux variations over the reactor core height. The primary governing equations for isotopic depletion and helium production are:

$$\frac{dN_{^{58}\text{Ni}}}{dt} = -\sigma_{^{58}\text{Ni}}^{\text{fast}}\phi_{\text{fast}}N_{^{58}\text{Ni}}, \tag{9}$$

$$\frac{dN_{^{59}\text{Ni}}}{dt} = \sigma_{^{58}\text{Ni}}^{\text{fast}}\phi_{\text{fast}}N_{^{58}\text{Ni}} - \sigma_{^{59}\text{Ni}}^{\text{thermal}}\phi_{\text{thermal}}N_{^{59}\text{Ni}}, \tag{10}$$

$$\frac{dN_{^{10}\text{B}}}{dt} = -\left(\sigma_{^{10}\text{B}}^{\text{thermal}}\phi_{\text{thermal}} + \sigma_{^{10}\text{B}}^{\text{fast}}\phi_{\text{fast}}\right)N_{^{10}\text{B}}, \tag{11}$$

where σ represents the microscopic cross-section for each reaction, ϕ is the neutron flux, and N is the atomic concentration of the isotope. The helium production rates are expressed as:

$$\frac{dN_{\text{He}}}{dt} = \sum \text{Contributions from all reactions.} \tag{12}$$

The cumulative helium production from various isotopes and the total production over time is presented in Figure 17, which was obtained by integrating the above equations numerically.
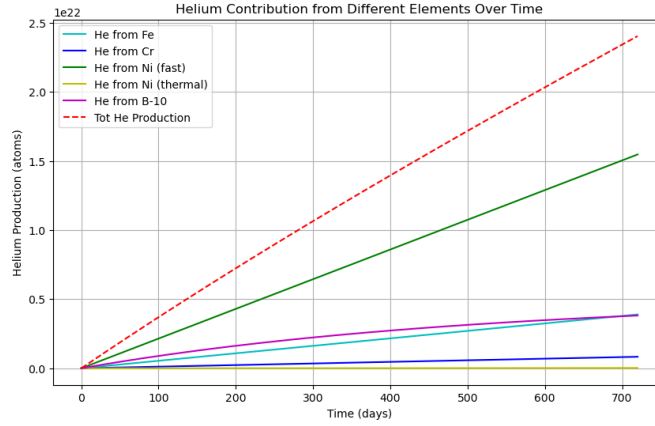

Figure 17: Helium contribution from different elements over time.

Assuming a conservative model where all helium remains trapped within the cladding material, the helium concentration after 1 year of operation is approximately 80 ppm, increasing to 152 ppm after 2 years.

10.2.2 Effects of Helium Embrittlement

Helium embrittlement arises due to helium accumulation at grain boundaries, leading to:

– Reduced ductility and toughness of the cladding.

– Increased susceptibility to crack initiation and propagation.

– Accelerated creep and swelling under high temperature and irradiation.

11 DESIGN RESULTS AND CONCLUSION

This section presents the design outcomes, their implications, and the conclusions drawn on the feasibility and safety of the proposed design.

11.1 Code

Following the verification process, the various pieces of code were adapted and integrated to ensure proper functionality. The resulting implementation was cross-checked against the

previous work to confirm that no unintended modifications or errors ("corruptions") occurred during the process.

The final code accepts cladding thickness and plenum height as input parameters and iteratively performs computations until the temperature map converges to a stable solution.

To determine the optimal values for these two quantities, a previously developed genetic algorithm was employed for dimensional optimization.

11.2 Findings and Considerations

During the dimensioning process, it was observed that the cladding thickness is strongly influenced by the operational time specified in the fitness function. For short cycles, such as one year, the algorithm tends to recommend a thinner cladding, which may not be suitable for long-term operation. To address this limitation, even though the task focused on a one-year design, the dimensioning was based on an expected four-year fuel cycle, which is more representative of typical fast reactor operation.

This conservative approach ensures improved reliability and provides additional safety margins over the lifecycle of the fuel pin.

It was also observed that the time to rupture depends on the height of the plenum. A lower plenum height leads to higher internal pressure, which in turn reduces the time to rupture. Consequently, the algorithm's optimization tends to converge towards the maximum plenum height and minimum cladding thickness within the specified exploration range.

Given these trends, additional considerations were taken into account:

– **Manufacturability and robustness**: A cladding that is too thin is challenging to manufacture and more susceptible to failure due to external factors.

– **Economic implications**: A higher plenum height increases the cost of production as it necessitates a taller reactor vessel.

To address these challenges, we adopted limits based on existing technology:

– **Cladding thickness**: 80 to 120 micrometers.

– **Plenum height**: 80 to 100 cm (approximately the same as the active fuel length).

11.3 Results

The design and verification process demonstrated that all critical parameters remain well within the specified limits.

The finalized design dimensions are as follows:

– **Cladding Thickness:** $90 \mu m$.

– **Plenum Height:** $1m$.

With the selected dimensions, we extended the computation to simulate an uptime of 2 years instead of the initial 1-year design. The results demonstrate the performance and safety of the fuel pin under prolonged operational conditions:

- **Maximum Fuel Temperature:** 2553.260 K (increased from 2480.096 K).

- **Maximum Cladding Temperature:** 912.696 K (unchanged).

- **Plenum Pressure:** 5.409 MPa (limit exceeded, increased from 2.792 MPa).

- **Maximum Instantaneous Cladding Plastic Strain:** 0.000% (unchanged).

- **Maximum Cladding Volumetric Swelling:** 20.118% (limit exceeded, increased significantly from 2.900%).

- **Maximum Coolant Velocity:** 5.558 m/s (increased from 4.779 m/s).

- **Minimum Gap Thickness:** 367.927 microns (decreased from 386.495 microns).

- **Burnup:** 128.268 GWd/tHM (increased from 64.134 GWd/tHM).

- **Fuel Yielding Due to Swelling:** 8.979% (increased from 4.489%).

- **Time to Rupture:** 4.23 years (decreased significantly from 51.98 years).

Comparison and Observations:

- The maximum fuel temperature increased slightly, indicating a higher thermal load on the fuel, likely due to increased burnup.

- The plenum pressure and cladding volumetric swelling both exceeded design limits, indicating that the fuel pin design is insufficient for extended irradiation cycles without adjustments.

- The burnup doubled, as expected

- The time to rupture decreased drastically from 51.98 years to 4.23 years, showing that thermal creep becomes a significant concern under these conditions.

- While the coolant velocity increased, it remained within acceptable operational ranges, highlighting that the thermal-hydraulic design is not a limiting factor in this scenario.

- The decreased gap thickness indicates increased mechanical interaction between the fuel and cladding, which can exacerbate the risks associated with swelling and fuel-cladding mechanical contact.

In summary, the significant rise in cladding swelling, plenum pressure, and reduced time to rupture indicate that this design requires further optimization to handle extended operation cycles safely.

APPENDIX

All of the code can be found in the following GitHub repository: NDT-Homeworks Repository.